

Modeling cell rheology with the Subcellular Element Model

Sebastian A Sandersius¹ and Timothy J Newman^{1,2}

¹ Department of Physics, Arizona State University, Tempe, AZ 85287, USA

² School of Life Sciences, Arizona State University, Tempe, AZ 85287, USA

Received 13 November 2007


Accepted for publication 14 February 2008

Published 9 April 2008

Online at stacks.iop.org/PhysBio/5/015002

Abstract

Recently, the Subcellular Element Model (SEM) has been introduced, primarily to compute the dynamics of large numbers of three-dimensional deformable cells in multicellular systems. Within this model framework, each cell is represented by a collection of elastically coupled elements, interacting with one another via short-range potentials, and dynamically updated using over-damped Langevin dynamics. The SEM can also be used to represent a single cell in more detail, by using a larger number of subcellular elements exclusively identified with that cell. We have tested whether, in this context, the SEM yields viscoelastic properties consistent with those measured on single living cells. Employing virtual methods of bulk rheology and microrheology we find that the SEM successfully captures many cellular rheological properties at intermediate time scales and moderate strains, including weak power law rheology. In its simplest guise, the SEM cannot describe long-time/large-strain cell responses. Capturing these cellular properties requires extensions of the SEM which incorporate active cytoskeletal rearrangement. Such extensions will be the subject of a future publication.

 This article features online multimedia enhancements

1. Introduction

1.1. The Subcellular Element Model

Understanding the biomechanical properties of cells and tissues presents a severe challenge to the modeling community. These systems display a wide range of rheological behaviors over multiple time scales. These properties ultimately derive from protein–protein interactions either pertaining to the cytoskeleton of individual cells or bridging membranes of neighboring cells. We do not have yet either the detailed knowledge nor computational power to simulate cell or tissue-level mechanics in terms of these microscopic interactions. It is assumed that a coarse-grained or phenomenological approach can be used for these larger length scales. Models at these scales will be described by coarse-grained degrees of freedom and effective parameters, some of which may be estimated from experimental measurements.

In modeling multicellular structures (such as tissues, tumors and embryos), one needs to account for the interactions between tens of thousands of cells, typically in a complex three-dimensional environment. A number of simulational

frameworks for multicellular systems have been proposed over the years [1]. It has proven particularly challenging to describe the three-dimensional morphologies of individual cells, and yet cell shape is a crucial aspect of both cell mechanics and cell behavior. The Subcellular Element Model (SEM) was introduced recently as an efficient off-lattice simulation algorithm for simulating thousands of cells in three dimensions, with the shape of each cell being an emergent output of the algorithm itself (rather than parameterized as an input) [3]. To allow adaptive cell shape in the SEM, individual cells are composed of hundreds of ‘elements’ which have short-range viscoelastic interactions. As illustrated in figure 1, the SEM has been shown to produce multicellular structures with an uncanny resemblance to real structures [2].

The main motivation for the work described in this paper is to understand whether the structures produced by the SEM (figure 1) are just ‘reminiscent’ of real biological structures or whether the SEM is capturing enough of the underlying biomechanics such that the properties of the SEM structures are relevant to the properties of the real biological systems. Our initial strategy is to analyze in detail the biomechanics which emerge from application of the SEM to a system of one single

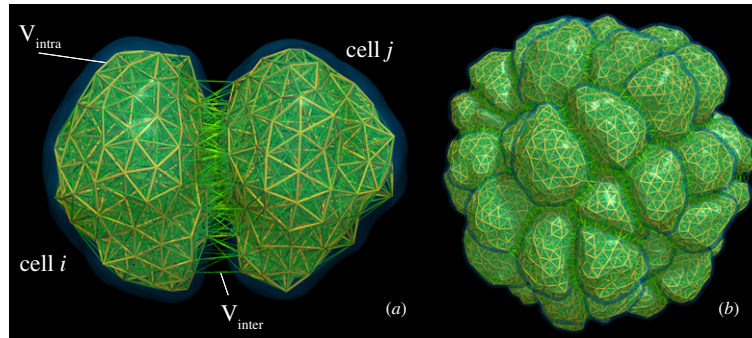


Figure 1. Visualization of multicellular structures formed by the SEM. Isosurfaces are shown here to identify each cell. Elements are located at the nodes between filaments while the filaments represent the interactions between the elements. Thick filaments roughly denote nearest neighbor interactions and increasingly thinner filaments roughly denote next-nearest interactions. (a) Two cells each with about 500 elements. Cells, inter-cellular and intra-cellular interactions are labeled corresponding to equation (1). (b) A spherical cluster of about 110 cells with about 370 elements per cell.

cell. The dynamics of single cell deformation is an important feature to consider in modeling. Single cell deformations can trigger differentiation, remodeling, migration, growth and gene expression [4, 5], and influence morphogenic dynamics at larger scales. If the SEM is able to capture, at a semi-quantitative level, the main features of single-cell rheology at intermediate time scales, it is plausible that the emergent cell shapes observed in multicellular simulations are faithful to the real cell morphologies observed in nature, which are themselves emergent from the multi-scale biomechanical interactions within and between cells. We do not address in this study the assumptions in the SEM concerning inter-cellular interactions.

The SEM can be motivated as follows. Consider the cytoskeleton of the cell, which is a fantastically complex network of dynamically cross-linked filaments. To describe this network at a coarse-grained level we imagine partitioning the cell into mesoscopic volumes (each with an approximate linear size of $1 \mu\text{m}$ —thus a cell of linear size $10 \mu\text{m}$ would be composed of approximately 10^3 such volumes). Each volume contains thousands of filaments. The common surface of two neighboring volumes will be penetrated by filaments close to that surface within each of the two volumes. We now consider a phenomenological description in which each volume is replaced by a node located at the volume’s center of mass, and the common filaments between the volumes are replaced by an effective elastic potential between the neighboring nodes. This potential should be Hookean for small deviations from equilibrium, strongly repulsive at short distances to model volume exclusion, and short-ranged in order to allow dynamical separation of neighboring nodes under larger-scale cell deformations—an explicit form for this potential will be given shortly. We term these nodes ‘subcellular elements’. In the simplest model, as discussed here, we impart over-damped dynamics to the elements; this represents the viscous drag experienced by the cytoskeletal subvolume in the intra-cellular cytoplasm. In principle there could also be dissipative interactions between elements within the cell, proportional to the relative velocity of elements. Such interactions are not considered here. We assume the effect of such interactions to be small compared to the effect obtained

solely from the absolute damping of each element with the cell cytoplasm. This is consistent with results obtained from simplified one-dimensional models [6]. In a multicellular system, especially a tissue (such as an epithelial sheet), cells will have strong biomechanical interactions with their neighbors. We describe these cell–cell interactions through element–element interactions between surface elements of neighboring cells. Again, a short-ranged elastic potential is used to represent these interactions. Here the inter-cellular potential is a phenomenological description of the membrane-bound junctions between the cells. This phenomenological coarse-grained model can also be used to describe non-cellular viscoelastic structures, such as extra-cellular matrix or non-biological amorphous materials.

Denoting individual cells by Roman indices, and elements by Greek indices, we may write the equation of motion for the position vector of a single element α_i in the form of the following Langevin equation:

$$\eta \dot{\mathbf{y}}_{\alpha_i} = \xi_{\alpha_i} - \nabla_{\alpha_i} \sum_{\beta_i \neq \alpha_i} V_{\text{intra}}(|\mathbf{y}_{\alpha_i} - \mathbf{y}_{\beta_i}|) - \nabla_{\alpha_i} \sum_{j \neq i} \sum_{\beta_j} V_{\text{inter}}(|\mathbf{y}_{\alpha_i} - \mathbf{y}_{\beta_j}|). \quad (1)$$

On the left-hand side, η is the damping constant originating from the viscous drag on an element from the surrounding cytoplasm. On the right-hand side, the noise term ξ_{α_i} is a Gaussian-distributed random variate with zero mean and correlation:

$$\langle \xi_{\alpha_i}^m(t) \xi_{\beta_j}^n(t') \rangle = 2D\eta^2 \delta_{i,j} \delta_{\alpha_i, \beta_j} \delta^{mn} \delta(t - t'), \quad (2)$$

where m and n are vector component labels in the three-dimensional space and D is a diffusion coefficient. This noise term is a coarse-grained description of molecular-level fluctuations of a mesoscopic region of cytoskeleton, originating from thermal noise and uncorrelated polymerization/depolymerization events. Correlated polymerization/depolymerization events, which are crucial for active cell motion and large-scale deformations, will not be considered in this paper, but can be implemented in the SEM framework by correlated creation and annihilation of elements. V_{intra} and V_{inter} are element–element interaction

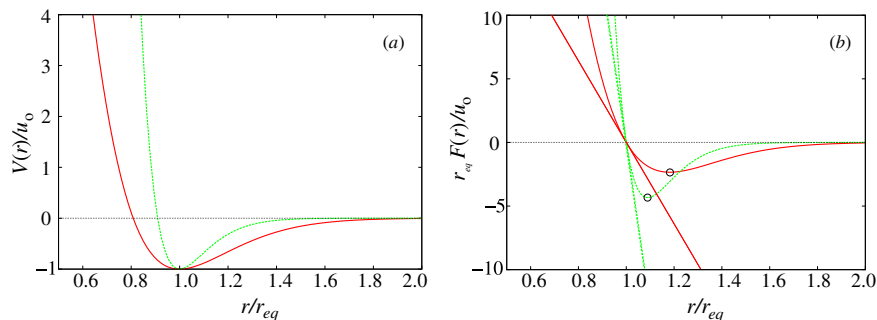


Figure 2. (a) The scaled interaction potential $V(r)$, as expressed in equation (4). The solid (dashed) line shows this potential with $\rho = 2.0(4.0)$. Note that increasing ρ pinches the potential well, which increases the strength of repulsion and decreases the range of attraction. (b) The scaled radial interaction force $F(r) = -\partial_r V(r)$. The solid (dashed) line corresponds to $\rho = 2.0(4.0)$. Note that increasing ρ moves the inflection point of the interaction potential, shown by round circles, closer to the equilibrium distance. The two tangent lines show the harmonic approximations for the two cases as expressed by equation (5).

potentials describing intra-cellular and inter-cellular interactions, respectively. An illustration showing these two types of element–element interactions is shown in figure 1(a). In a non-biological application, V_{inter} could also be used to model heterogeneous aggregates. We have written the SEM at the lowest level of complexity in which element–element interactions are isotropic and elements are identical in their mechanical properties. Naturally, heterogeneous elements and/or anisotropic potentials can be used in more detailed models of specific cell properties.

Given that the purpose of this paper is to examine the viscoelastic properties of a single cell, we can drop the Roman indices and discard the inter-cellular potential, thus simplifying the Langevin equation to

$$\eta \dot{\mathbf{y}}_\alpha = \xi_\alpha - \nabla_\alpha \sum_{\beta \neq \alpha} V_{\text{intra}}(|\mathbf{y}_\alpha - \mathbf{y}_\beta|). \quad (3)$$

In our rheological ‘computer experiments’ it will be necessary to perturb some elements, and to hold others fixed, thus simulating deformations with external forces.

Hereafter, we shall refer to V_{intra} simply as V . We take V to have the following form, which is illustrated in figure 2(a):

$$V(r) = u_0 e^{2\rho(1-\frac{r^2}{r_{eq}^2})} - 2u_0 e^{\rho(1-\frac{r^2}{r_{eq}^2})}. \quad (4)$$

Here, u_0 is the depth of the potential well, r_{eq} is the equilibrium distance of the potential well and ρ is a scaling factor. This potential is reminiscent of the Morse potential commonly used to describe intra-molecular forces. The precise functional form of the potential has no qualitative impact on the emergent properties of the system, so long as the same energy and length scales are used. We choose to write the exponential terms as Gaussian functions as these provide a rapidly decaying potential written purely in terms of the squared distance r^2 (useful for optimized computer implementation). For small deviations about the equilibrium distance the elastic coupling of the interaction can be approximated by a linear spring, with spring constant κ , given by the following expression:

$$\kappa = \frac{8\rho^2 u_0}{r_{eq}^2}. \quad (5)$$

Considering briefly a system of just two elements, and using the harmonic approximation, equation (3) can be

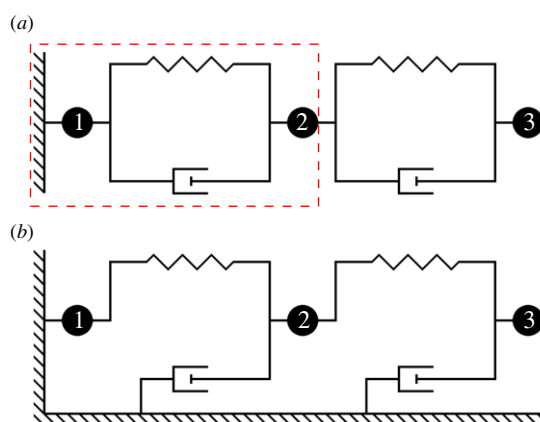


Figure 3. (a) A system of two Kelvin–Voigt bodies connected in series. A single Kelvin–Voigt body shown outlined is constructed of a dashpot and spring in parallel configuration. A dashpot has a damping force proportional to the velocity of deformation, and a spring has an elastic force proportional to deformation. (b) The respective system but with damping relative to the medium as represented with the SEM in equations (1) and (3).

simplified to

$$\eta \dot{\mathbf{y}}_1 = \xi_1 - \kappa(\mathbf{y}_1 - \mathbf{y}_2), \quad (6)$$

with a similar equation for \mathbf{y}_2 . In the absence of noise, this equation of motion is very similar to that of an isolated viscoelastic system known as the Voigt model or Kelvin model, illustrated in figure 3(a). A Kelvin–Voigt model is a phenomenological viscoelastic body consisting of a linear elastic spring and a linear viscous dashpot in a parallel configuration. More details on the viscoelastic properties of the Kelvin–Voigt model can be found in appendix A. One might think that the SEM is a generalized, multi-node Kelvin–Voigt model in three dimensions. However this is not the case. With the Kelvin–Voigt model, the damping force felt by an element is dependent on its relative velocity with neighboring elements. As already discussed, in equations (1) and (3) the damping force on an element is dependent only on its relative velocity with the reference frame of the cell. This difference between the SEM and a generalized Kelvin–Voigt model is illustrated in figure 3.

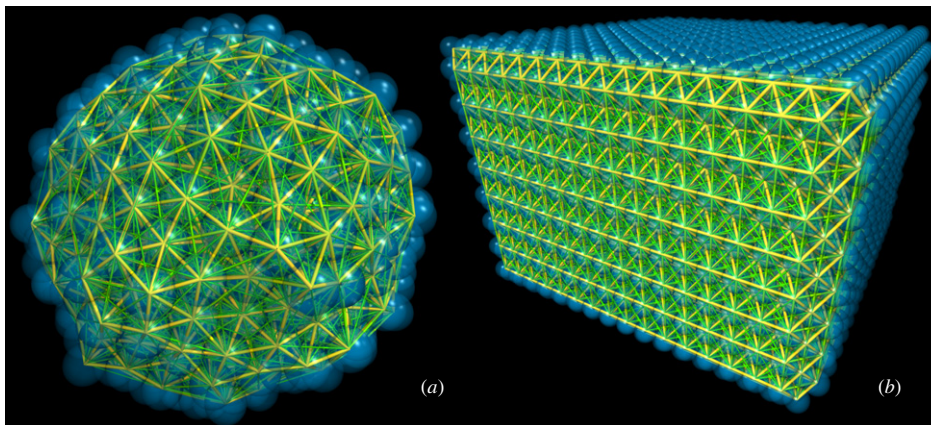


Figure 4. Visualization of structures formed by the SEM. Spheres represent the elements with a radius $r_{\text{eq}}/2$ and filaments represent the interactions between the elements. Thick filaments roughly denote nearest neighbor interactions and increasingly thinner filaments roughly denote next-nearest interactions. (a) An aggregate of 1024 elements which were initialized in random positions, but relatively close proximity. The elements have equilibrated into a random amorphous viscoelastic network with an overall macroscopic spherical shape. (b) A close-packing arrangement of 5161 elements.

1.2. The equilibrated single cell

Using the phenomenological potential equation (4), N elements randomly placed in close proximity will equilibrate into an amorphous spherical shape as shown in figure 4(a). This is also shown in supplemental movie 1. The elements can also be systematically placed into ordered close-packing arrangements as shown in figure 4(b). In these arrangements the elements are in a metastable state of equilibrium and they will rearrange to minimize surface area if thermal fluctuations are sufficiently large. For the amorphous arrangement the aggregate of elements forms an approximately spherical ‘cell’ of radius R_{cell} . By regarding the elements as closely packed uniform spheres, we can relate the cell radius to the inter-element distance via

$$p_3 \frac{4}{3} \pi R_{\text{cell}}^3 = N \frac{4}{3} \pi \left(\frac{r_{\text{eq}}}{2} \right)^3. \quad (7)$$

Here p_3 is a three-dimensional packing density (of spheres), N is the number of elements and r_{eq} is the equilibrium distance of the interaction potential. We can use this expression to set the scale for r_{eq} for given values of R_{cell} and N .

From equation (7) we have

$$r_{\text{eq}}(N) = 2R_{\text{cell}} \left(\frac{p_3}{N} \right)^{\frac{1}{3}}. \quad (8)$$

For randomly packed spheres it has been shown that the packing density is $p_3 = 0.64$ [7]. For a highly efficient uniform sphere packing arrangement, cubic close packing or hexagonal close packing for example, the packing density is $p_3 = \pi/3\sqrt{2} \cong 0.7405$ [8]. The subcellular elements have a mutual attraction for each other and are weakly compressible. As we shall see below, their equilibrated packing will be of higher efficiency than that of randomly packed spheres.

To further understand what a reasonable value for the packing density p_3 may be for a given system, we measured the probability distribution of element–element interaction

distances for all interacting elements in an equilibrated aggregate. In particular, we use the pair distribution function

$$P(r) = \frac{1}{M} \sum_{m=1}^M \frac{1}{N^2} \sum_{\beta \neq \alpha} \delta(|\mathbf{y}_\alpha(m\delta t) - \mathbf{y}_\beta(m\delta t)| - r). \quad (9)$$

We stress that in the above expression r is not a measure of radial distance within the cell, but, rather, denotes the separation between two elements. This function is defined as a discrete time average over the stochastic dynamics for a given realization. We perform time averaging as opposed to ensemble averaging because of the significant time required to equilibrate each realization prior to measuring $P(r)$. We show measurements for five different realizations in figure 5 and there are no significant sample–sample fluctuations. $P(r)$, for a 256 element cell, is shown in figure 5(a). The two sets of curves correspond to two different values for the scaling factor ρ (which appears in the interaction potential, equation (4)). The set of curves which are highly peaked at $r = r_{\text{eq}}$ corresponds to $\rho = 4.0$, and the other set corresponds to $\rho = 2.0$. Figure 5(b) is similar, but gives results for a cell consisting of 1024 elements.

The differences between figures 5(a) and (b) arise from, in the case of different element quantities, the effects of averaging over more surface elements relative to the number of bulk elements. The interacting pair distribution shows, for $\rho = 4.0$, that the packing density of the equilibrated elements is roughly that of closely packed arrangements of uniformly-sized hard spheres. For uniform close-packing arrangements, the nearest neighbor and next-nearest neighbor distances are (in units relative to the diameter of the spheres) 1, $\sqrt{2} \simeq 1.4142$, $\sqrt{3} \simeq 1.7321$ and 2. As figure 5 shows, for $\rho = 4.0$, the interacting pair distributions are clearly peaked at around 1, $\sqrt{3}$ and 2, and slightly peaked at around $\sqrt{2}$. The barely resolved peak just below $\sqrt{3}$ can be explained by the next-nearest neighbor distance of the closely packed triangular dipyrmaid which is $2\sqrt{6}/3 \simeq 1.6329$. The broadness of the peaks indicates that the equilibrated elements are not in lattice configurations.

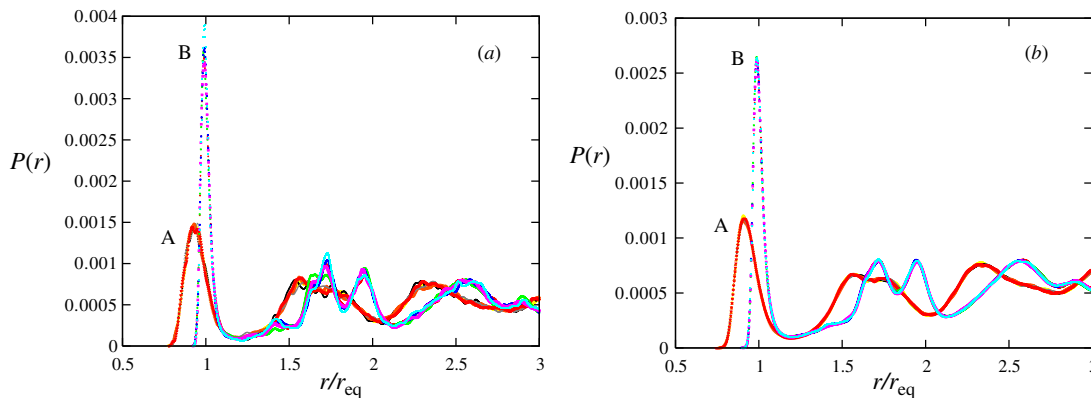


Figure 5. Pair distribution functions of all interacting elements within equilibrated aggregates of 256 elements (a) and 1024 elements (b). For both (a) and (b), sets of curves labeled A and B denote aggregates with element–element interaction potentials using $\rho = 2.0$ and $\rho = 4.0$, respectively. In each case, pair distributions are measured for five different equilibrated aggregates. It is clear that sample fluctuations are minimal.

Though the elements are densely packed, the aggregate is amorphous. For $\rho = 2.0$, the interacting pair distribution is indicative of a more compressed aggregate of relatively softer spheres. In comparison to the data for $\rho = 4.0$, one can see that for $\rho = 2.0$ the nearest neighbor peak is much broader, with a maximum peak at r/r_{eq} a little less than 1. The next-nearest neighbor peaks are not resolved. The reason for these differences can be traced to the distance dependence of the inter-element forces, as illustrated in figure 2(b). For $\rho = 4.0$, the attractive force decays more rapidly than for $\rho = 2.0$. Also, the repulsive force is greater for $\rho = 4.0$ than for $\rho = 2.0$. The weaker repulsion for separations less than r_{eq} and stronger attraction for separations greater than r_{eq} cause greater self-compression of the $\rho = 2.0$ aggregates.

There may be biological significance in varying the scaling factor ρ , that being cytoskeletal prestress, which is a compressive force caused by tensile forces from activity of molecular motors. This is thought to create rigidity or stiffness to the cytoskeletal network in the cell. It has been shown that this prestress may have a major effect on cell elasticity [9]. In the SEM framework, lowering the value for ρ effectively increases prestress in the simulated cell.

2. Scaling the viscoelastic network

The subcellular elements allow us to simulate the cell, but of course they are not biological entities. Therefore, it is crucial that measurable properties of the cell, as simulated using the SEM, do not depend on the number of elements used. As we explain in more detail below, varying the number of elements (N) in the cell, without scaling the SEM parameters with N in some fashion, will quantitatively change rheological characteristics, such as bulk elasticity and viscosity. In this section we motivate two scaling laws—one for the effective spring constant between neighboring elements and the other for the element damping constant. These are sufficient to ensure that, so long as N is reasonably large (about 100 or greater), biomechanical properties of the SEM cell are independent of N .

To start the discussion, consider a simple one-dimensional example: the effective elasticity of springs placed in series. If N identical Hookean springs, each with a spring constant κ , are placed in series, then the effective spring constant for the collection of springs is $\kappa_{\text{eff}} = \kappa/N$. If one requires that the effective spring constant be independent of N , then one must scale the individual spring constants by N . Now consider three-dimensional elastic networks, where we will require that the effective elastic modulus be independent of N (which we now take to be the number of nodes or subcellular elements). For configurations in which elements have short-range interactions, we argue below that, for large N , the elastic modulus should scale as $N^{1/3}$. Consider a three-dimensional elastic network of macroscopic fixed length scale l_0 , with the N elements positioned in a cubic lattice configuration. If the N elements are connected by identical springs, with spring constants κ , the elastic modulus (without considering a Poisson's ratio for volumetric change) is

$$\frac{\sigma}{\varepsilon} = \frac{N^{2/3} \kappa}{N^{1/3} - 1 l_0}, \quad (10)$$

where we have written the elastic modulus as the ratio of stress σ to strain ε . This relation is derived in appendix B.

Beyond the simple cubic configuration, and especially for more complex elastic networks, it becomes very tedious or impossible to find exact expressions relating the elastic modulus of the network to the pairwise elasticity and number of constituent building blocks. A cell, as modeled by the SEM, will be formed from an amorphous network of elements; as such we use an approximate scaling relation, namely the scaling relationship for the cubic lattice network, but with an adjustable parameter λ to tune the leading correction to scaling. Using equation (10), we scale the pairwise elasticity (i.e. the spring constant for small deviations from equilibrium between two elements) as

$$\kappa = \kappa_0 N^{-1/3} (1 - \lambda N^{-1/3}). \quad (11)$$

We must also scale the viscous damping constant. The damping of N elements scales linearly with N , so we use the scaling relation

$$\eta = \eta_0 N^{-1}. \quad (12)$$

Using equation (11) with equation (5), we scale the elastic coupling at the equilibrium distance accordingly and use this to compute u_0 for the element–element interaction potential. Now, for a given N , η_0 and κ_0 (and hence u_0) can be set so that the bulk viscoelastic properties of the collection of elements will have the desired elastic stiffness and time scale for deformation dynamics. To estimate a value κ_0 consider the elastic properties of a living cell, which has an elastic modulus on the order of 100–1000 Pa [10–12]. Combining equations (10) and (11), this indicates that the elastic modulus of the SEM network will be on the order of κ_0/l_0 , where l_0 is about $10\ \mu\text{m}$. From this we find that κ_0 should have a value on the order of 10^{-3} – $10^{-2}\ \text{N m}^{-1}$. To estimate a value for η_0 we consider the time scale over which the Kelvin–Voigt model transitions from a fluid to a solid. This is given by η_0/κ_0 , and is comparable, for a living cell, to a time scale of about 1 s [11, 13, 14]. Therefore η_0 should have a value on the order of 10^{-3} – $10^{-2}\ \text{N s m}^{-1}$.

3. Methods

3.1. Measuring bulk rheology

In order to measure the bulk rheology, we equilibrate an SEM cell within two parallel planes, which represent the plates used in experiments to which the cell membrane can adhere [11, 12]. The element–boundary interaction is computed only in the direction perpendicular to the plane, and the potential describing this interaction uses the same parameter values as the element–element interaction potential, thus minimizing the effect of the boundaries on the rheological properties of the system. The upper boundary is free to move and the lower one is fixed. The equilibration of this system creates an aggregate of elements with two parallel, relatively flat surfaces of elements adhering to the boundaries, as shown in figure 6(a). We will refer to these flat surfaces of elements as slabs. The upper slab is free to move (in unison with the boundary) and the lower one is fixed. The elements making up these slabs will be used to strain the bulk or perturb the macroscopic shape of the aggregate. To control the applied stress, we compute the surface area of the upper slab, A_{slab} , and count the number of elements in the slab, N_{slab} . Each element in the upper slab has applied to it a force of magnitude $f_{\text{ext}} = F_{\text{ext}}/N_{\text{slab}}$. The applied stress has a magnitude $\sigma = F_{\text{ext}}/A_{\text{slab}}$. By varying the direction of the applied force, the cell can be subjected to tensile stress, shear stress or other types of external perturbation. To match the measurement protocol of recent cell rheology experiments [12, 13], we employ uniaxial stretching with constant stress: to ensure this, the upper slab elements are allowed to move only in the direction of the applied forces. Supplemental movies 2 and 3 visualize uniaxial stretching, with constant applied stress, of 256 and 1024 element aggregates, respectively.

3.2. Measuring microrheology

To understand the rheological properties of the material at the microscopic level, we perturb a single element within the

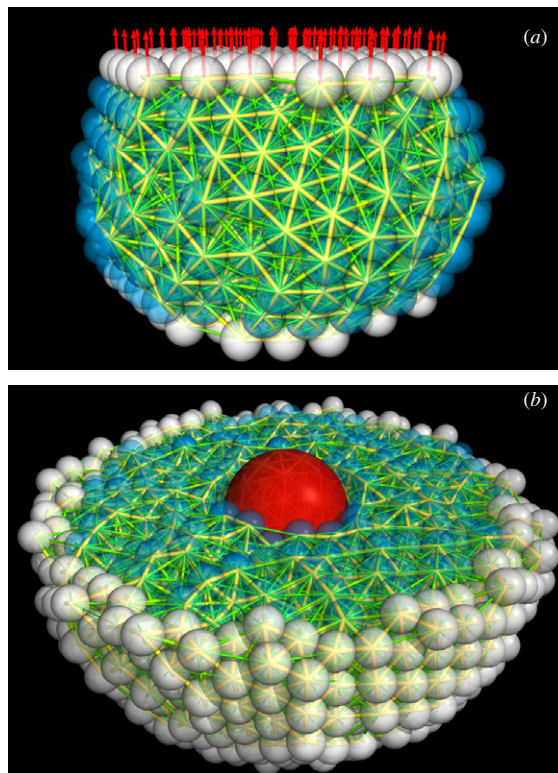


Figure 6. Methods of measuring bulk rheology and microrheology in the SEM. (a) 1024 elements equilibrated between two boundaries. The macroscopic shape of the aggregate has two relatively flat surfaces of ‘slab’ elements, shown in white (both slabs have the same degree of ‘flatness’ though this is not obvious from the perspective shown). These slabs are used to measure the macroscopic properties of the bulk. In this case to stretch the bulk, the bottom slab is fixed and the top slab is pulled upward with a constant applied stress. Red arrows indicate the uniform force vectors applied to each individual element within the top slab. (b) A hemispherical cross-section of a 4096 element aggregate equilibrated with a bead in the bulk. The bead, shown in red, is used to probe the local properties of the system. Once the aggregate and bead are equilibrated, the outer surface elements, shown in white, are fixed.

bulk and measure its response, which is mediated in a non-trivial manner through interactions with surrounding elements in the cell. The perturbed element represents the magnetic bead used in these types of microrheology experiments on single cells [10, 15]. In order to properly probe the properties of the material in this way, it is necessary to fix the outer surface elements of the cell; otherwise the perturbations will cause an overall global cell motion that will obscure the local response to the perturbation. Referring to figure 6(b), the fixed surface elements are shown in white, while the unconstrained bulk elements are shown in blue. The perturbed element is colored red.

Using the magnetic bead microrheology protocol established by Lutz *et al* [16], we apply an oscillatory force to the bead and compute the storage modulus $G'(\omega)$, and loss

modulus $G''(\omega)$, with the following expressions:

$$G'(\omega) = \frac{f_0}{g|x_0(\omega)|} \cos[\phi(\omega)],$$

$$G''(\omega) = \frac{f_0}{g|x_0(\omega)|} \sin[\phi(\omega)].$$
(13)

Here, f_0 is the amplitude of an oscillatory driving force, ω is the driving frequency, $x_0(\omega)$ is the amplitude of displacement of the perturbed bead and $\phi(\omega)$ is the phase shift between the driving force and bead displacement. The geometric prefactor g is determined by the surrounding strain field of the perturbed bead. Since the bead is spherically symmetric we approximate the geometric prefactor to be that of a sphere: $g = 6\pi R_b$ where R_b is the radius of the spherical bead. The interaction potential between the bead and the elements is different to the element–element interaction potential. We represent the bead as a non-adhesive hard sphere, and use the following repulsive potential for the bead–element interaction:

$$V_b(r) = u_b e^{2\rho_b(1-\frac{r}{R_b})}. \quad (14)$$

The stiffness of the bead κ_b at $r = R_b$ is given by

$$\kappa_b = \frac{4u_b\rho_b(4\rho_b - 1)}{R_b^2}. \quad (15)$$

We must also specify a separate reference frame damping constant for the bead, which we denote by η_b . Supplemental movie 4 visualizes this bead microrheology, showing oscillatory perturbation on a bead within the bulk of a 4096 element aggregate.

4. Results

4.1. Results for bulk rheology

The first bulk measurement we report is creep response. For a material, creep is the temporal deformation in response to a constant applied stress. We apply such a constant stretching stress to an aggregate of elements equilibrated between two boundaries, as illustrated in figure 6(a). Visualizations showing examples of this with 256 and 1024 element aggregates can be seen, respectively, in supplemental movies 2 and 3. We use the following system parameters: scaling parameter for spring constant $\kappa_0 = 5.0 \times 10^{-3} \text{ N m}^{-1}$, scaling parameter for damping $\eta_0 = 5.0 \times 10^{-3} \text{ N s m}^{-1}$, diffusion coefficient $D = 1.6 \times 10^{-13} \text{ m}^2 \text{ s}^{-1}$. The parameters of the interaction potential, equation (4), were: $\rho = 2.0$, u_0 as computed by equation (5) in combination with equation (11) with $\lambda = 0.75$ and $r_{\text{eq}} = 2.85 \mu\text{m}$ as computed from equation (8) with $N = 256$, $R_{\text{cell}} = 10 \mu\text{m}$ and $p_3 = \pi/3\sqrt{2}$. We measured a creep strain for different values of constant applied stress ranging from about 7 Pa to 20 Pa (figure 7). The creep strain curves show that for small applied stress there is (i) a macroscopic deformation which is finite on long time scales and (ii) total recovery after stress release. This is much like the creep for the Kelvin–Voigt model as described in appendix A. Also note that the creep plateaus at around 1 s, which is consistent with the ratio $\eta_0/\kappa_0 = 1 \text{ s}$. These measurements match quantitatively well

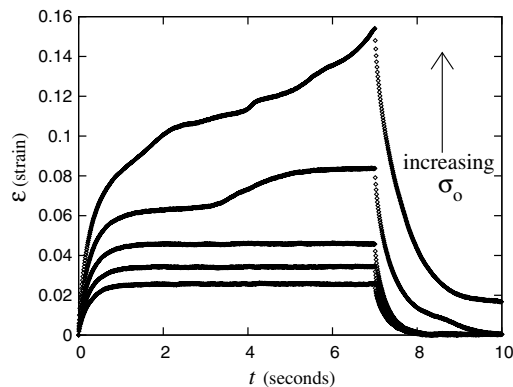


Figure 7. Creep strain versus time with constant stress applied to an aggregate of 256 elements. The different curves show measurements for different values of constant stress applied from $t = 0$ to $t = 7 \text{ s}$. The constant stresses applied were 6.59 Pa, 8.66 Pa, 11.40 Pa, 15.00 Pa and 19.75 Pa. For small applied stress we see finite deformations on long time scales with a total recovery after stress release. Above a deformational strain of about 0.1, the aggregate starts to flow or break apart and does not show total recovery after stress release.

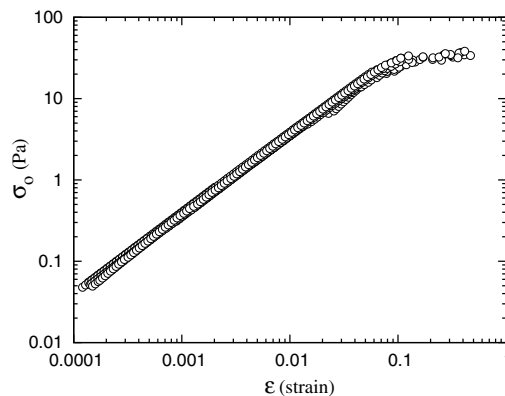


Figure 8. Stress versus strain for eight different equilibrated aggregates of 256 elements on a log–log scale. The curves are consistent with a power law of unity and an elastic modulus of $360 \pm 19 \text{ Pa}$ for strain below about 0.1. Thus, the aggregates have a macroscopic elasticity which is Hookean for small strain. Above 10% strain, the elasticity decreases showing breakage or plasticity.

with intermediate time scale, low strain creep measurements done by Wottawah *et al*; specifically when they applied a constant stress of 15 Pa for a period of 2.5 s [13]. For larger applied stress, there is a macroscopic deformation which is plastic for long time scales. This can be seen more clearly from the stress versus strain curve (figure 8). These measurements were taken from eight different equilibrated aggregates of 256 elements with constant stresses ranging from about 0.05 Pa to 30 Pa. The stress versus strain curves show that the aggregates have an elastic modulus of $360 \pm 19 \text{ Pa}$, which is Hookean below a strain of about 0.1. Above this strain value, the aggregates break apart. This critical strain value emerges from a microscopic property of the aggregates, namely that the element–element interaction potential (equation (4)) has an inflection point, shown by circles, at about $r/r_{\text{eq}} = 1.1$. This

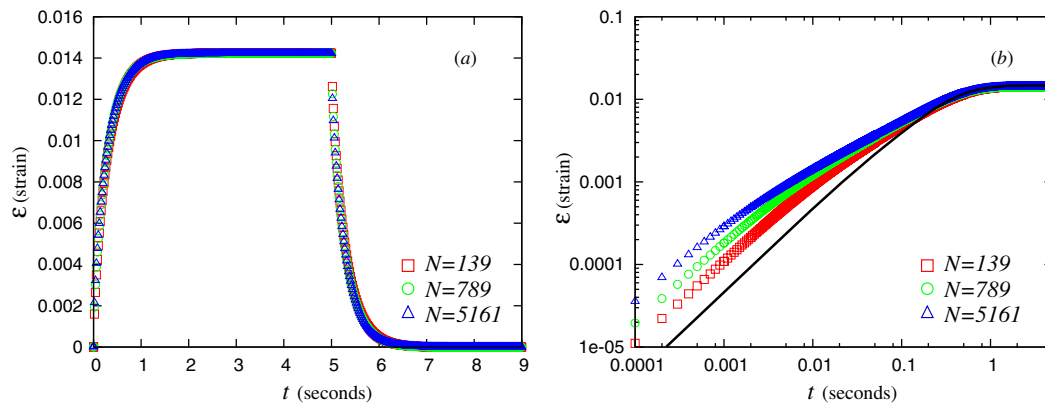


Figure 9. Creep strain curves for different sized systems of the 14:10 ordered structure with $\lambda = 0.5$. (a) With the same constant stress of 5.0 Pa applied from $t = 0$ to $t = 5$ s, the creep strain curves for $N = 139$, 789 and 5161 overlap well. (b) Shown in log–log scale, it is apparent that the trajectories do not overlap in the shorter time regime. The solid black curve shows the creep strain for the Kelvin–Voigt model which has a single time scale η/κ for the fluid–solid transition (appendix A).

can be seen clearly from the relative maxima, shown by circles, in the force curves shown in figure 2(b). Thus, when a pair of interacting elements is being stretched apart, once their mutual separation is beyond this inflection point the force which has moved them from equilibrium to this point will overpower the element–element elastic restoring force, resulting in the pair breaking apart. This microscopic property scales up to give the macroscopic property of plasticity for larger strain.

4.1.1. Scaling ordered viscoelastic networks. To test the scaling relations discussed in section 2 we employed bulk measurements on deterministic ordered viscoelastic networks using the block shaped arrangement as shown in figure 4(b). Following the same procedures outlined in section 3.1, we measured macroscopic stress and strain relations for networks constructed of elements whose elasticity was scaled by equation (11) and viscosity scaled by equation (12). For equation (11), we found that $\lambda = 0.5$ gives the best scaling results. The parameter settings for the following results were: $\kappa_0 = 5.0 \times 10^{-3} \text{ N m}^{-1}$, $\eta_0 = 5.0 \times 10^{-3} \text{ N s m}^{-1}$. The parameters of the interaction potential, equation (4), were: $\rho = 4.0$, u_0 as computed by equation (5) in combination with equation (11) (with $\lambda = 0.5$) and r_{eq} computed for various system sizes and arrangements. We have used $\rho = 2.0$ for all measurements in this paper, except for those made on ordered viscoelastic networks: $\rho = 4.0$ is used for these because this reduces next-nearest neighbor interactions and avoids the stable but warped block shapes that otherwise occur with the choice $\rho = 2.0$. For the system size of the arrangements, an initial height was set as $10 \mu\text{m}$. We used an aspect ratio of roughly 14:10 (width to height) for the network. To vary the number of elements which make up the structure we varied the number of lateral lattices from 5, then 9 and finally 17, which correspond to $N = 139$, 789, 5161, respectively.

As stated, we found that $\lambda = 0.5$ works best for scaling the microscopic elasticity. This is illustrated with the creep strain curves for different sized systems in figure 9. Shown in log–log scale, figure 9(b), we can see that the trajectories

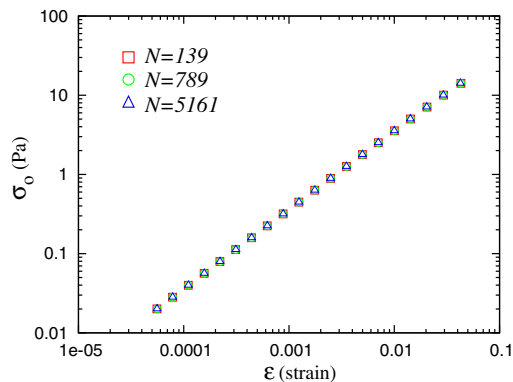


Figure 10. Stress versus strain with $\lambda = 0.5$ for three different values of N . The elastic modulus is relatively size invariant with N . The elastic modulus is measured to $357 \pm 4 \text{ Pa}$.

do not overlap for the shortest time scale. These short time scales of less than 1 s are biologically irrelevant in the context of bulk rheology experiments. In the following subsection on microrheology results we show that scaling is good over a wide range of time scales and that ‘weak power law’ rheology, as observed in cells for frequencies around 1–10 Hz, is reproduced in the SEM.

Given that good scaling was achieved for the creep curves using $\lambda = 0.5$, we used this value in our measurement of stress versus strain curves for the different values of N (figure 10). The measured elastic modulus was found to be independent of N as desired, and to have a value of $357 \pm 4 \text{ Pa}$.

4.1.2. Scaling random viscoelastic networks. We have shown in section 4.1.1 that the scaling relations, equations (12) and (11), work quite well with $\lambda = 0.5$ for deterministic ordered aggregates of elements (figure 4(b)). We now examine whether these scaling relations hold for random amorphous aggregates of elements, such as those shown in figures 4(a) and 6(a).

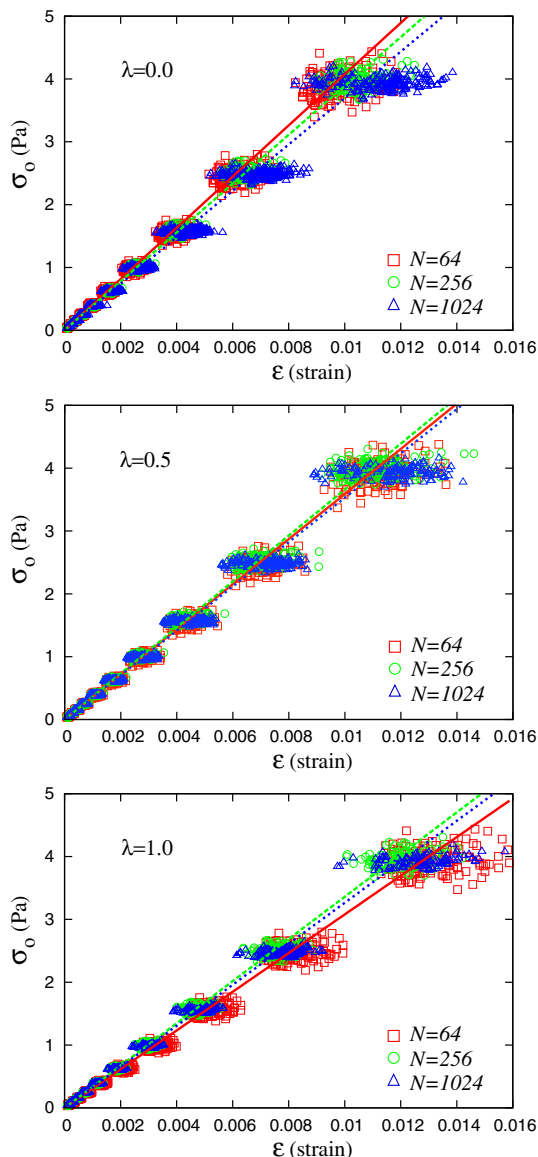


Figure 11. Stress versus strain curves for multiple amorphous aggregates of different sizes: $N = 64, 256$ and 1024 . Measuring the elastic modulus from these data points as shown in table 1, we see that the macroscopic elastic modulus is scale invariant with N , within sampling error, if λ is about 0.5. This is consistent with the most effective value of λ found for scaling ordered networks.

We employed bulk measurements on random amorphous networks, using the method outlined in section 3.1. The parameter values used were $\kappa_0 = 5.0 \times 10^{-3} \text{ N m}^{-1}$ and $\eta_0 = 5.0 \times 10^{-3} \text{ N s m}^{-1}$. The parameters of the interaction potential, equation (4), were: $\rho = 2.0, u_0$ as computed from equation (5) in combination with equation (11) for various λ and r_{eq} as computed from equation (8) with various $N, R_{\text{cell}} = 10 \mu\text{m}$ and $p_3 = \pi/3\sqrt{2}$. We worked with three different system sizes: $N = 64, 256$ and 1024 . Since the arrangement of elements is different for every randomly initiated aggregate, the macroscopic properties of the bulk will not be exactly reproducible (for finite N). Thus, in order

Table 1. Values for the measured elastic modulus (in units of Pa), for different sized systems for various values of λ as shown in figure 11.

N	$\lambda = 0.0$	$\lambda = 0.5$	$\lambda = 1.0$
64	407 ± 16	359 ± 11	308 ± 9
256	389 ± 12	366 ± 13	336 ± 7
1024	370 ± 24	354 ± 18	326 ± 8

to assess the correct scaling relation, we measured stress versus strain curves for 100 different equilibrated aggregates, for each given system size. This was repeated for three values of λ : 0.0, 0.5 and 1.0. Reviewing the results of these measurements as shown in figure 11, we see there is significant sample-to-sample fluctuations in the aggregate stiffness. The measurements of the elastic modulus from these stress–strain curves are shown in table 1. Within the sample-to-sample fluctuations, the scaling relation, equation (5), works well for $\lambda = 0.5$.

4.2. Results for microrheology

Finally, we present measurements of microrheology in a cell described by the SEM. We measure the storage and loss moduli, following the procedures outlined in section 3.2. The parameter values used were $\kappa_0 = 5.0 \times 10^{-3} \text{ N m}^{-1}$, $\eta_0 = 5.0 \times 10^{-3} \text{ N s m}^{-1}$. The parameters of the element–element interaction potential equation (4) were $\rho = 2.0, u_0$ as computed by equation (5) in combination with equation (11) with $\lambda = 1.0$ and r_{eq} as computed from equation (8) with various $N, R_{\text{cell}} = 10 \mu\text{m}$ and $p_3 = \pi/3\sqrt{2}$. We use $\lambda = 1.0$ as supposed to 0.5 simply because these measurements were made before we discovered that $\lambda = 0.5$ produces better scaling behavior. The microrheology measurements required significant computer time to produce, and it was deemed unnecessary to repeat them for $\lambda = 0.5$, since, as discussed below, good scaling was found for $\lambda = 1.0$. We worked with three different system sizes: $N = 256, 1024$ and 4096 . The parameters of the element–bead interaction potential, equation (14), were $\rho_b = 4.0, u_b$ as computed by equation (15) with $\kappa_b = 2.67 \times 10^{-4} \text{ N m}^{-1}$ and $r_b = 3.0 \mu\text{m}$. For the reference frame viscosity of the bead η_b we used a value of $5.0 \times 10^{-6} \text{ N s m}^{-1}$; evaluating Stoke’s formula for a sphere in a viscous medium, this is about 100 times larger than the viscosity of water at 37°C . Perturbing the bead with a 10pN amplitude driving force f_0 , we oscillated the bead with driving frequencies ranging from $\omega/2\pi = 0.1 \text{ Hz}$ to 10^4 Hz . With this driving force amplitude, the maximum trajectory amplitude x_0 was about 5 nm and was reached at driving frequencies greater than 1 Hz. Supplemental movie 4 shows an example of oscillatory perturbation on a bead within the bulk of a 4096 element aggregate. For each system size, we measured the storage modulus $G'(\omega)$ and the loss modulus $G''(\omega)$ as shown in figure 12. Because the elements interacting with the bead are not isotropically arranged around the bead, we investigated the strength of anisotropy by measuring $G'(\omega)$ and $G''(\omega)$ for bead oscillations in the x, y and z directions. From figure 12 one sees that anisotropy has an observable effect (since the fixed cell boundary elements are not isotropically distributed),

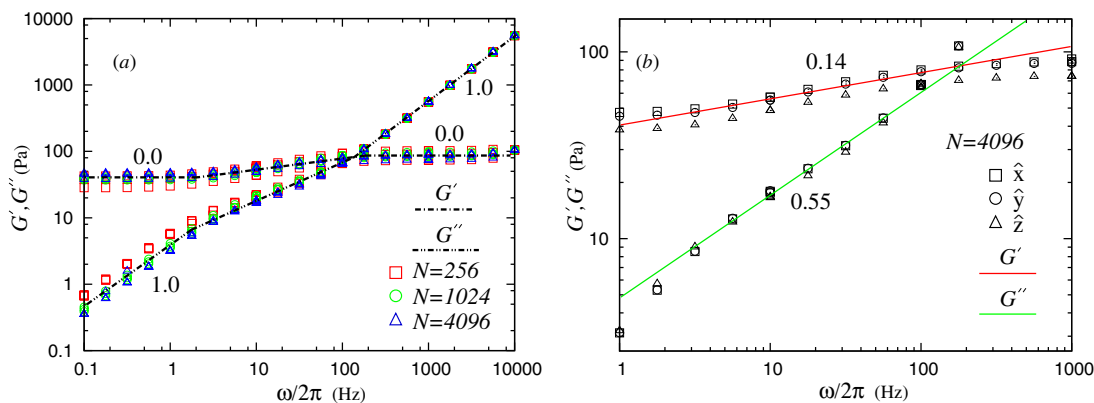


Figure 12. Measurements of the storage modulus $G'(\omega)$ and the loss modulus $G''(\omega)$ in the x , y and z directions for three different system sizes ($N = 256$, 1024 and 4096) (a). In common with the Kelvin–Voigt model $G'(\omega)$ is constant in the long and short time regimes and $G''(\omega)$ has a power law of one in the long and short time regimes. In the intermediate time regime, as shown in closer view with the x , y , z data for $N = 4096$ in (b), it can be seen that $G'(\omega)$ has a weak apparent power law with exponent 0.14 ± 0.02 and $G''(\omega)$ has an apparent power law with exponent 0.55 ± 0.05 .

but decreases as N gets larger. This is expected, since in the limit that $N \rightarrow \infty$, the stress field which the elements pose on the bead becomes isotropic. It is clear from figure 12 that scaling with N is reasonable. $G'(\omega/2\pi < 1\text{Hz})$ plateaus to a value of about 40Pa; comparing this to the results from bulk rheology, this is one order of magnitude smaller than the macroscopic elastic modulus. Qualitatively, the storage and loss moduli are similar to those calculated for the Kelvin–Voigt model (appendix A). For short time scales $G''(\omega)$ dominates and for long time scales $G'(\omega)$ dominates. In the intermediate time regime $G'(\omega)$ and $G''(\omega)$ have apparent power laws, with the weak power law exponents 0.14 ± 0.02 and 0.55 ± 0.05 , respectively. These effective exponents have been observed in cell rheology experiments [17, 15]. It is possible that these weak power laws arise from many-body viscoelastic interactions – we intend to pursue this connection in future work.

5. Discussion and conclusion

We have measured both bulk and microrheological properties of aggregates (both ordered and amorphous) using the SEM. We have shown how to make the viscoelastic properties scale invariant with respect to the total number of interacting elements (N)—this is an essential property of the SEM as the subcellular elements are a modeling device, and measurable quantities must not depend on N . Estimating parameter values in the scaling laws, equations (11) and (12), we showed that the aggregates of elements had an elastic modulus with the same order of magnitude as that measured for living cells [10–12]. For strain below 10%, the characteristics of the creep curve matched those for the Kelvin–Voigt model. Above strain of 10%, the aggregates show characteristics of flow or plastic breakage. With this, the model lacks cellular characteristics when it comes to high strain deformations. Desprat *et al* and Micoulet *et al* report being able to stretch cells to strain values of around 4–6 before cell rupture. Comparing our results with experimental whole cell creep measurements [12, 13],

the model does not show characteristics of flow over long time scales. This is expected, as the simplest version of the SEM, as studied here, has no processes modeling active rearrangement of cytoskeleton. Creep measurements of high strain over long time scales from Desprat *et al* showed a creep compliance which behaved as a power law for strain below 1 over a time scale of hundreds of seconds. However, creep measurements of small strain over an intermediate time scale by Wottawah *et al* match quite well with our results, specifically when they applied a constant stress of 15 Pa for a period of 2.5 s. Over long time scales, intra-cellular activity starts to affect the rheological properties of the cell. At a given instant in time, the cell is a watery bag of organelles shrouded by a vast entangled network of semi-flexible polymers interlocked with cross-linkers [18]. Because of these cross-linkers, as a non-active material, the cell should show dynamic properties of being a viscoelastic solid over long time scales [19]. It is believed that intra-cellular activity such as cytoskeletal reconstruction is the reason the cell shows fluidity on long time scales [12, 14].

Another attribute of cell behavior is active contraction under a residual external force following prior extension of the cell [11]. A similar effect has also been observed for cells stressed by a sustained external force (Atef Asnacios, personal communication). Dynamic stiffening is another cell response stimulated by mechanical perturbation. This stiffening need not involve contraction. Although not known to be an active or passive response of the cytoskeleton, Fernández *et al* have shown that a force above a cell-dependent critical value can induce a transition from linear viscoelastic behavior to power law stress stiffening [20]. Recent measurements reported by Trepal *et al* strongly indicate that stiffening, in part, is an active response of the cell [21]. By performing a macroscopic transient pulse extension (stretch–unstretch) on the cell, they microrheologically measured a cytoskeletal response of prompt fluidization followed by slow resolidification on the time scale of hundreds of seconds. Interestingly, the rate of stiffening was found to be dependent

on the ATP available to the cell: ATP-depleted cells showed a dramatically slower resolidification rate. Fluidization response, however, was found to be independent of ATP availability. Cytoskeletal dynamics and cell response to mechanical stimulus, whether passive or active, continue to bemuse the scientific community and much has yet to be understood—especially when classifying these properties with cell type. These properties have not been considered in this paper but are being studied in our group, using extensions of the SEM which phenomenologically incorporate more sophisticated cytoskeletal dynamics.

In comparing our microrheology measurements with experiment measurements performed on living cells, we find broad qualitative agreement. The SEM does not reproduce the 3/4 scaling for G' and G'' in the high frequency regime. This is an emergent property of semi-flexible polymer networks [19] that has recently been observed in living cells [15]. The SEM is designed to capture whole cell/tissue properties and contains no basic polymer physics, which is essential to capture high frequency behavior. Microrheology measurements performed here *in silico* on the SEM elucidate a mechanism which may play a role in the emergence of weak power law rheology on intermediate timescales [22]—something which is observed in real cells [17, 15, 23]. In the same spirit as the theoretical model from Balland *et al.*, we find that weak power law rheology emerges from many relaxation times inherent to the material (figures 9(b) and 12). Our findings show that this intermediate time regime/weak power law rheology can emerge due to structure alone and not necessarily due to structural rearrangements as propounded by the theory of soft-glass rheology (SGR) [23, 24]. Because the SEM is a three-dimensional network, the multiple orientations of viscoelastically interacting elements (figure 6) create the multiple relaxation times which are needed for intermediate time regime/weak power law rheology to emerge.

6. Outlook

As mentioned in the introduction, the original motivation for the SEM was to simulate large three-dimensional multicellular clusters of deformable cells (as illustrated in figure 1). In this paper, we have shown that the cells that make up these structures are not simply ‘cartoons’ of real cells. The SEM is able to capture, in a semi-quantitative manner, the intermediate-frequency rheology of living cells. This strengthens our confidence in (i) using the SEM as a cutting-edge computational tool for multicellular systems and (ii) introducing new biological features into the model, that can account for more sophisticated cell behavior beyond simple (non-active) mechanics, and tailoring the model for a variety of cell types. As a next step we plan to introduce targeted element decay, growth and structural rearrangement to model active cytoskeletal dynamics underpinning cell mechanics such as active motility, polarity and long-time/large-strain responses. Another short-term goal is to interface the SEM biomechanics with numerical simulation of intra-cellular biochemical kinetics. This is an important step to allow closer connection to cell biology experiments, and is an important

goal for the modeling community as a whole, regardless of which particular simulation framework/algorithm is utilized.

Acknowledgments

SS gratefully acknowledges informative discussions with Atef Asnacios, Albrecht Ott and Jeffrey Fredberg. The authors would like to thank Bruce J A Nourish for IT development and administration. This work was partially supported by awards NSF IOB-0450680 and NSF/NIH DMS/NIGMS-0342388.

Appendix A

We consider here the viscoelastic properties of the Kelvin–Voigt model, the equation of motion for which is written as

$$\eta \dot{\mathbf{y}} = -\kappa \mathbf{y} + \mathbf{F}_{\text{ext}}. \quad (\text{A.1})$$

Viscosity is given by η and elasticity is given by κ . Solving this differential equation with constant force \mathbf{F}_{ext} , and with initial conditions $\dot{\mathbf{y}}(t=0) = \mathbf{y}(t=0) = 0$, we find the following creep function:

$$\mathbf{y}(t) = \frac{\mathbf{F}_{\text{ext}}}{\kappa} (1 - e^{-\frac{\kappa}{\eta}t}). \quad (\text{A.2})$$

We note that this is a one-dimensional system even though the terms are boldfaced (representing vectors). Because of this, the creep compliance is $J(t) = \mathbf{y}(t)/\mathbf{F}_{\text{ext}}$:

$$J(t) = \frac{1}{\kappa} (1 - e^{-\frac{\kappa}{\eta}t}). \quad (\text{A.3})$$

Within the linear viscoelastic regime [25], the complex modulus $G^*(\omega)$ is related to the creep compliance by the following expression:

$$G^*(\omega) = \frac{1}{i\omega \hat{J}(\omega)}. \quad (\text{A.4})$$

The storage modulus $G'(\omega)$ and the loss modulus $G''(\omega)$ are equal to the real and imaginary parts of the complex modulus:

$$G^*(\omega) = G'(\omega) + iG''(\omega). \quad (\text{A.5})$$

Loosely speaking, $G'(\omega)$ captures elastic properties and $G''(\omega)$ captures viscous properties of the viscoelastic model. In equation (A.4), $\hat{J}(\omega)$ is the Fourier transform of $J(t)$ which is defined as

$$\hat{J}(\omega) = \int_{-\infty}^{\infty} J(t) e^{-i\omega t} dt. \quad (\text{A.6})$$

Because $J(t) = 0$ for $t < 0$, we obtain

$$\hat{J}(\omega) = \frac{1}{\kappa} \int_0^{\infty} e^{-i\omega t} dt - \frac{1}{\kappa} \int_0^{\infty} e^{-(\frac{\kappa}{\eta} + i\omega)t} dt. \quad (\text{A.7})$$

Evaluating this integral, we find (for $\omega \neq 0$)

$$\hat{J}(\omega) = \frac{1}{i\omega\eta(i\omega + \kappa/\eta)}, \quad (\text{A.8})$$

Using equation (A.4) we can now get the complex modulus:

$$G^*(\omega) = \kappa + i\eta\omega. \quad (\text{A.9})$$

From this it is trivial to separate the real and imaginary parts to obtain the storage and loss moduli:

$$G'(\omega) = \kappa, \quad G''(\omega) = \eta\omega. \quad (\text{A.10})$$

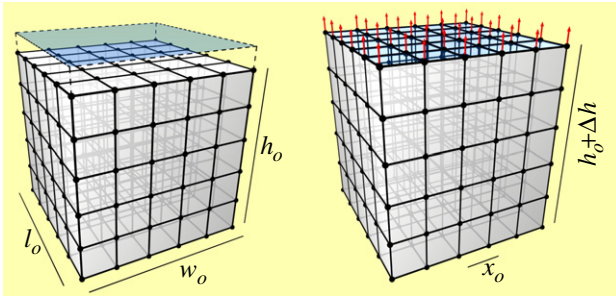


Figure 13. A cubic lattice of N elements elastically coupled to nearest neighbors by Hookean springs of equilibrium length x_0 . With a stress applied to the top surface area (outline by a translucent plane), the elastic network deforms with a change in height Δh .

As we can see from this, $G'(\omega)$ is a constant and $G''(\omega)$ is linearly dependent on ω . This tells us that the Kelvin–Voigt model is more of a fluid for high frequency (short time domain) and more of a solid for low frequency (long time domain). The frequency scale for which the model transitions from a fluid to a solid, $G'(\omega_0) = G''(\omega_0)$, is given by $\omega_0 = \kappa/\eta$.

Appendix B

Consider an elastic network of N elements elastically coupled in cubic lattice configuration (figure 13). The elements are elastically coupled by uniform springs of linear elasticity κ and with equilibrium length x_0 . Though the local lattice configuration is cubic, the macroscopic shape of the network is taken to be cuboidal, with length l_0 , width w_0 and height h_0 . The total number of elements is $N = n_l n_w n_h$. Accordingly,

$$\begin{aligned} l_0 &= x_0(n_l - 1), & w_0 &= x_0(n_w - 1), \\ h_0 &= x_0(n_h - 1). \end{aligned} \quad (\text{B.1})$$

To stretch the object, the bottom surface elements are fixed and a force F_0 is applied to each of the top surface elements. These forces, shown as vector arrows in figure 13, when applied to the top surface area create a stress:

$$\sigma = \frac{n_l n_w F_0}{l_0 w_0}. \quad (\text{B.2})$$

With a stress applied to the top surface of the network, a strain $\varepsilon = \Delta h/h_0$ will result. Using Hooke's law and realizing that in a single column there are $n_h - 1$ springs, we have

$$F_0 = \frac{\kappa}{n_h - 1} \Delta h. \quad (\text{B.3})$$

Following from this and substituting equation (B.3) into equation (B.2), the elastic modulus is

$$\frac{\sigma}{\varepsilon} = \frac{n_l n_w}{(n_h - 1)} \frac{h_0 \kappa}{l_0 w_0}. \quad (\text{B.4})$$

Considering the case of a symmetric macroscopic shape in which $n_l = n_w = n_h$ and $l_0 = w_0 = h_0$, the elastic modulus simplifies to

$$\frac{\sigma}{\varepsilon} = \frac{N^{\frac{2}{3}}}{N^{\frac{1}{3}} - 1} \frac{\kappa}{l_0}. \quad (\text{B.5})$$

Glossary

Cytoskeleton. A vast network of biopolymers giving the eukaryotic animal cell structural stability, and which together with the regulation of associated proteins enables an array of mechanical functions not limited to: division, motility and intra-cellular motion.

Langevin equation. Named after physicist Paul Langevin, the Langevin equation is a stochastic differential equation naturally incorporating microscopic fluctuations with deterministic mesoscopic dynamics.

Kelvin–Voigt model. Named after physicists Baron Kelvin (William Thomson) and Woldemar Voigt, the Kelvin–Voigt body is a phenomenological model used to quantitatively describe viscoelastic materials.

Rheology/microrheology. Rheology is the study of the deformation and flow of matter. Microrheology is specifically the study of deformation and flow of the microscopic constituents of a material.

Off-lattice simulation. A class of simulation methods in which the position vectors of the fundamental objects (e.g. atoms, subcellular element, cells, etc) are not constrained to an underlying grid. Such methods allow efficient simulation of three-dimensional systems and avoid possible artifacts which may arise from an imposed grid.

References

- [1] Anderson A, Chaplain M and Rejniak K (ed) 2007 *Single Cell Based Models in Biology and Medicine* (Basle: Birkhäuser)
- [2] Newman T J 2007 Modeling multicellular structures using the subcellular element model *Single Cell Based Models in Biology and Medicine* ed A Anderson, M Chaplain and K Rejniak (Basle: Birkhäuser) pp 221–39
- [3] Newman T J 2005 Modeling multi-cellular systems using sub-cellular elements *Math. Biosci. Eng.* **2** 611–22
- [4] Ingber D E 2006 Mechanical control of tissue morphogenesis during embryological development *Int. J. Dev. Biol.* **50** 255–66
- [5] Vogel V and Sheetz M 2006 Local force and geometry sensing regulate cell functions *Nat. Rev. Mol. Cell Biol.* **7** 265–75
- [6] Newman T J and Sandersius S A 2007 unpublished
- [7] Jaeger H M and Nagel S R 1992 Physics of granular states *Science* **255** 1523–31
- [8] Steinhaus H 1999 *Mathematical Snapshots* 3rd edn (New York: Dover) pp 202–03
- [9] Wang N, Tolic-Norrelykke I M, Chen J, Mijailovich S M, Butler J P, Fredberg J J and Stamenovic D 2002 Cell prestress: I. Stiffness and prestress are closely associated in adherent contractile cells *Am. J. Physiol. Cell Physiol.* **282** 606–16
- [10] Bausch A R, Möller W and Sackmann E 1999 Measurement of local viscoelasticity and forces in living cells by magnetic tweezers *Biophys. J.* **75** 2038–49
- [11] Micoulet A, Spatz J P and Ott A 2005 Mechanical response analysis and power generation by single-cell stretching *Chem. Phys. Chem.* **6** 663–70
- [12] Desprat N, Richert A, Simeon J and Asnacios A 2005 Creep function of a single living cell *Biophys. J.* **88** 2224–33

- [13] Wottawah F, Schinkinger S, Lincoln B, Ananthkrishnan R, Romeyke M, Guck J and Käs J 2005 Optical rheology of biological cells *Phys. Rev. Lett.* **94** 098103
- [14] Kasza K E, Rowat A C, Liu J, Angelini T E, Brangwynne C P, Koenderink G H and Weitz D A 2006 The cell as a material *Curr. Opin. Cell. Biol.* **19** 101–7
- [15] Deng L, Treppe X, Butler J P, Millet E, Morgan K G, Weitz D A and Fredberg J J 2006 Fast and slow dynamics of the cytoskeleton *Nat. Mater.* **5** 636–40
- [16] Lutz R J, Litt M and Chakrin L W 1973 Physical–chemical factors in mucus rheology *Rheology of Biological Systems* ed H L Gabelnick and M Litt (Springfield: Thomas) pp 119–57
- [17] Hoffman B D, Massiera G, Van Citters K M and Crocker J C 2006 The consensus mechanics of cultured mammalian cells *Proc. Natl Acad. Sci. USA* **1033** 10259–64
- [18] Alberts B, Bray D, Lewis J, Raff M, Roberts K and Watson J 1994 *Molecular Biology of the Cell* (New York: Garland) pp 907–82
- [19] Morse D C 1998 Viscoelasticity of concentrated isotropic solutions of semiflexible polymers: 2. Linear response *Macromolecules* **31** 7044–67
- [20] Fernández P, Pullarkat P A and Ott A 2006 A master relation defines the nonlinear viscoelasticity of single fibroblasts *Biophys. J.* **90** 3796–805
- [21] Treppe X, Deng L, An S S, Navajas D, Tschumperlin D J, Gerthoffer W T, Butler J P and Fredberg J J 2007 Universal physical responses to stretch in the living cell *Nature* **447** 592–5
- [22] Stamenovic D 2006 Two regimes, maybe three? *Nat. Mater.* **5** 597–8
- [23] Balland M, Desprat N, Icard D, Frol S, Asnacios A, Browaeys J, Hnon H and Gallet F 2006 Power laws in microrheology experiments on living cells: comparative analysis and modeling *Phys. Rev. E* **74** 021911
- [24] Lenormand G and Fredberg J J 2006 Deformability, dynamics, and remodeling of cytoskeleton of the adherent living cell *Biorheology* **43** 1–30
- [25] Findley W N, Lai J S and Onaran K 1976 *Creep and Relaxation of Nonlinear Viscoelastic Materials* (Amsterdam: North-Holland) pp 50–107